A Bayesian Approach to Segmentation with Noisy Labels via Spatially Correlated Distributions

Ryu Tadokoro[1], Tsukasa Takagi[2], and (✉)Shin-ichi Maeda[2]

[1] Tohoku University, Japan `tadokororyuryu@gmail.com`
[2] Preferred Networks, Inc., Japan `{takagi,ichi}@preferred.jp`

Abstract. In semantic segmentation, the accuracy of models heavily depends on the high-quality annotations. However, in many practical scenarios such as medical imaging and remote sensing, obtaining true annotations is not straightforward and usually requires significant human labor. Relying on human labor often introduces annotation errors, including mislabeling, omissions, and inconsistency between annotators. In the case of remote sensing, differences in procurement time can lead to misaligned ground truth annotations. These label errors are not independently distributed, and instead usually appear in spatially connected regions where adjacent pixels are more likely to share the same errors. To address these issues, we propose an approximate Bayesian estimation based on a probabilistic model that assumes training data includes label errors, incorporating the tendency for these errors to occur with spatial correlations between adjacent pixels. Bayesian inference requires computing the posterior distribution of label errors, which becomes intractable when spatial correlations are present. We represent the correlation of label errors between adjacent pixels through a Gaussian distribution whose covariance is structured by a Kac-Murdock-Szegö (KMS) matrix, solving the computational challenges. Through experiments on multiple segmentation tasks, we confirm that leveraging the spatial correlation of label errors significantly improves performance. Notably, in specific tasks such as lung segmentation, the proposed method achieves performance comparable to training with clean labels under moderate noise levels. Code is available at https://github.com/pfnet-research/Bayesian_SpatialCorr.

Keywords: Segmentation · Noisy label · Noisy annotation · Bayesian inference · Spatial correlation.

1 Introduction

Semantic segmentation, which involves classifying each pixel in an image into one of several classes, is a crucial task in computer vision. In supervised learning, the accuracy of segmentation models critically depends on the quality of the annotations in the training data. However, obtaining truly accurate pixel-level annotations is challenging in many practical applications. Even when expert annotators are employed, errors, omissions, and subjectivity in interpretation are inevitable, leading to inconsistencies in datasets. In particular, high

inter- and intra-annotator variability is widely reported in medical imaging, where experts may have differing interpretations of the same structures. For instance, [41,19,27,38,27] highlight significant discrepancies among expert annotators; some delineate structures more generously, while others prefer more conservative annotations. The observer-dependent annotations exacerbate label noise in supervised learning. Label noise is also a critical issue in remote sensing, where determining ground truth labels often requires field surveys over large and sometimes inaccessible regions [7,26,6]. Due to the logistical and economic challenges of large-scale ground truth collection, researchers frequently rely on automatic labeling systems, which may introduce systematic errors. Additionally, high-quality annotated datasets remain a critical bottleneck for supervised learning, particularly in remote sensing applications where annotations are often repurposed across different types of satellite images. For example, the OpenEarthMap dataset [35] was created by manually annotating high-resolution optical satellite images for semantic segmentation. However, these annotations are sometimes reused for synthetic aperture radar (SAR) imagery, despite differences in resolution and capture conditions [12,42,23]. Additionally, changes in artificial structures or variations in land cover further contribute to label inconsistencies [8,12].

Various approaches have been proposed to mitigate the adverse effects of noisy labels. Some methods attempt to stop training early to prevent the network from overfitting to noise and generating unreliable pseudo-labels [21,22], while others modify the loss function to be more robust against large errors [9]. Although these techniques can reduce the influence of noisy annotations, they do not fundamentally address the core reason why the standard supervised learning framework fails in the presence of noisy labels.

We propose a method that directly tackles the root cause of this issue. In supervised learning for segmentation models, training typically reduces to optimizing the cross-entropy loss. This optimization implicitly follows a maximum likelihood estimation (MLE) framework under the assumption that the training data consists of independent and identically distributed samples drawn from the joint distribution of images and clean labels. However, when labels are noisy, the assumption of identically distributed assumption no longer holds, as the observed labels systematically deviate from clean labels, leading to performance degradation in the trained model.

To address this issue, we maintain the MLE framework but reformulate it using a more suitable probabilistic model. Specifically, we introduce a model that explicitly accounts for the presence of noisy labels, which differ from the clean labels due to labeling errors. In practice, annotation errors tend to exhibit strong spatial correlations - mislabeling often occurs in contiguous regions. Variations in annotation criteria among experts, as well as changes in the underlying scene — such as the construction or demolition of buildings or alterations in vegetation — further reinforce this spatial dependency. Given this, we assume that label errors are not independent but instead exhibit spatial correlations among pixels.

However, directly modeling spatial correlations poses significant computational challenges. To address this, we introduce a class of discrete distributions called the ELBO Computable Discrete Distribution, which enables the efficient optimization of the Evidence Lower Bound (ELBO). This discrete distribution is represented through continuous variables that follow a Gaussian distribution, where spatial correlations between pixels are expressed via a covariance matrix. Representing discrete variables through a Gaussian distribution successfully circumvents the intractability of summing over all possible realizations of the discrete variables. While the covariance matrix, whose number of elements scales quadratically with the number of pixels, introduces additional computational challenges in evaluating the ELBO, particularly in computing second-order statistics, its inverse, and its determinant. To overcome these computational intractabilities, we leverage the Kac-Murdock-Szegö (KMS) matrix [5,17], which enables efficient computations necessary for ELBO evaluation. To validate the effectiveness of our approach, we conduct extensive empirical evaluations on multiple segmentation tasks. Our experimental results demonstrate that our method significantly improves robustness against label noise, particularly in scenarios with moderate to high levels of spatially correlated label noise. In summary, our contributions are as follows:

1. **A probabilistic model with the ELBO Computable Discrete Distribution for learning with spatially correlated label noise:**
   We propose a probabilistic model that explicitly accounts for noisy labels and their spatial correlations, which are prevalent in real-world applications, particularly in medical imaging and remote sensing. To address the computational challenges of modeling spatially correlated label noise, we introduce the *ELBO Computable Discrete Distribution*, which represents discrete variables via continuous variables following a Gaussian distribution. This approach circumvents the computational difficulties caused by correlated discrete random variables while preserving spatial dependencies in label errors.

2. **Efficient ELBO optimization via the KMS matrix:**
   Computing the covariance matrix in our probabilistic model is computationally intractable due to the number of elements scaling quadratically with the number of pixels. We overcome this challenge by leveraging the KMS matrix, which enables efficient computation of second-order statistics, matrix inversion, and determinant evaluation - key operations necessary for ELBO optimization.

3. **Extensive empirical validation:**
   We perform comprehensive experiments on multiple segmentation tasks, demonstrating that our method significantly improves robustness to label noise. Our approach outperforms existing techniques, particularly in scenarios with moderate to high levels of spatially correlated label noise, validating the effectiveness of our probabilistic formulation.

2   Related Work

Learning with noisy labels has been a significant focus in the field of machine learning, particularly classification tasks [25,40,10,34]. One research direction models the relationship between the clean label y^* and the noisy label y through a transition matrix [25,40] that characterizes the probabilities from the clean label to the noisy label. For example, the transition probability from a clean label of k to a noisy label of j is represented as $p(y = j|y^* = k)$. Additionally, methods have been proposed to estimate an instance-dependent transition matrix [36,2], where the transition probabilities depend on the instance x also, denoted as $p(y = j|y^* = k, x)$. These classification methods can be adapted for semantic segmentation tasks; however, they treat label errors as being independent to each pixel, thereby ignoring the spatial correlations in label errors that may be present in annotations. This limitation is particularly critical in applications such as medical imaging [41,29,43] and remote sensing [24,31,21,11], where different types of noise may occur.

Other lines of research includes work by Zhang *et al.* [44], which proposed a Tri-Network framework that trains three networks simultaneously, with each pair selecting reliable pixels based on their loss maps, thereby achieving robust learning even with coarse annotations. Liu *et al.* [22] introduced a mechanism to detect the moment when a network begins to overfit noisy labels. Gonzalez *et al.* [9] designed T-Loss based on a Student-t distribution to apply a logarithmic penalty on large errors, reducing undue influence from outlier pixels. Nonetheless, these methods do not take into account the spatial correlations in label errors that may occur within annotations.

Unlike the aforementioned related works, there are few studies that consider spatial correlations. Li *et al.* [20] leveraged superpixel segmentation to group pixels and smooth the network outputs within each superpixel, thereby indirectly incorporating spatial context. This method, however, relies heavily on the quality of the generated superpixels. More recently, Yao *et al.* [39] proposed an approach that explicitly models spatial correlations by applying a Markov process that consists of expansion and shrinkage steps of the annotation masks. Although this method achieves better performance, it is mainly limited to addressing noise along the boundaries. In real-world scenarios, segmentation labels are often corrupted by a diverse range of noise types, including omission noise, misalignment noise, boundary uncertainties, and other systematic labeling errors [15,33,21,24,14].

Our proposed probabilistic model can incorporate spatial correlations in label errors without making assumptions about the noise types, thereby handling a wide range of noise types.

Logit of Label Error
(Unknown)
η

Noisy Label
y

Clean Label
(Unknown)
y^*

Input Image
x

(a)

Example 1   Example 2

$\rho = 0$

$\rho = 0.25$

$\rho = 0.75$

(b)
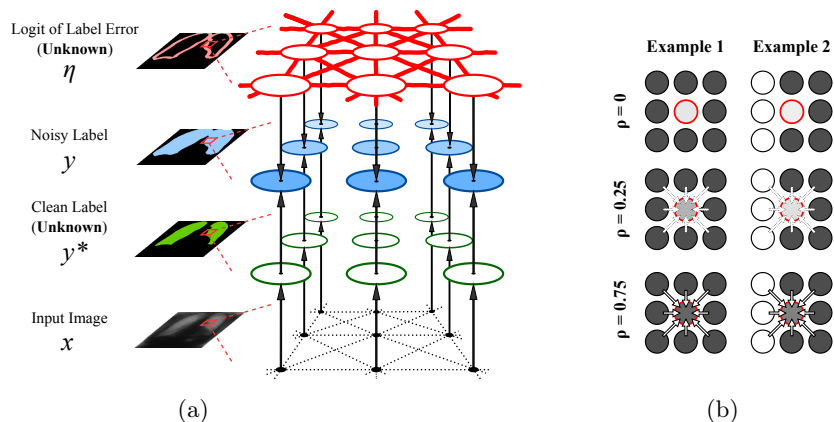
Fig. 1: **(a) Graphical model of the proposed model.** Our proposed method introduces a latent Gaussian variable η that encodes spatial correlations of label error among adjacent pixels, thereby enabling a more realistic modeling of the dependency between pixels.
(b) Conceptual illustration of spatial correlation. Examples 1 and 2 show how varying ρ affects the correlation strength between the center pixel and its neighbors (top, bottom, sides, and diagonals). When adjacent pixels are likely to contain label errors and spatial correlation is strong (ρ is high) label errors can be inferred with high confidence, even if they are rare.

3   Proposed Method

3.1   Overview

In supervised learning, training a segmentation model typically involves optimizing the cross-entropy loss. The optimization of cross-entropy loss implicitly assumes that the labels in the training data are independent and identically distributed samples drawn from the joint distribution of images and clean labels. However, this assumption about the probabilistic model does not accurately reflect reality. To address this, we explicitly model the relationship between noisy labels and clean labels by introducing clean labels that are distinct from the given noisy labels within a probabilistic framework that captures their plausible dependencies. By learning the segmentation model parameters through marginal likelihood maximization, which integrates out unknown latent label errors, we aim to mitigate the impact of label noise. Since direct maximization of the marginal likelihood is intractable, we approximate it via ELBO maximization [3,16], simultaneously estimating the approximate posterior distribution of label errors. By explicitly formulating a probabilistic model that accounts for label errors, the derived ELBO naturally leads to a well-justified loss function. Specifically, it includes the optimization of a cross-entropy loss computed using the estimated clean labels, where the contribution of each estimated clean label is

weighted according to its associated uncertainty. The following describes the probabilistic model we have constructed.

Let $\mathcal{Y}$ be a set of labels, $\mathbf{x} \in \mathbb{R}^{HW \times C}$ be an input image, $\mathbf{y} \in \mathcal{Y}^{HW}$ be an observed label, $\mathbf{y}^* \in \mathcal{Y}^{HW}$ be a clean label, and $\boldsymbol{\theta}$ be the parameters of the semantic segmentation model. The likelihood of the observed label $p(\mathbf{y}|\mathbf{x}, \boldsymbol{\theta})$ is defined as follows:

$$p(\mathbf{y}|\mathbf{x}, \boldsymbol{\theta}) = \sum_{\mathbf{y}^*} p(\mathbf{y}|\mathbf{y}^*) p(\mathbf{y}^*|\mathbf{x}, \boldsymbol{\theta}) = \sum_{\mathbf{y}^*} p(\mathbf{y}|\mathbf{y}^*) \prod_i p_{\boldsymbol{\theta}}(y_i^*|\mathbf{x}). \tag{1}$$

As mentioned in Section 1, real-world label errors such as omission and variation in expert annotation styles tend to exhibit spatial correlations. However, directly incorporating spatial correlations into discrete label variables makes computation intractable. To address this, we introduce a continuous variable, $\boldsymbol{\eta} \in \mathbb{R}^{HW}$, which is the logit of label error probability for each pixel that captures spatial correlations and indirectly imposes spatial dependencies on the labels as follows:

$$p(\mathbf{y}|\mathbf{y}^*) = \int p(\mathbf{y}|\mathbf{y}^*, \boldsymbol{\eta}) p(\boldsymbol{\eta}) d\boldsymbol{\eta} = \int \left\{ \prod_i p(y_i|y_i^*, \eta_i) \right\} p(\boldsymbol{\eta}) d\boldsymbol{\eta}. \tag{2}$$

Figure 1a depicts a graphical model illustrating this assumption. Here, $p(\boldsymbol{\eta})$ is modeled as a Gaussian distribution $p(\boldsymbol{\eta}) = \mathcal{N}(\boldsymbol{\eta}|\boldsymbol{\mu}, \boldsymbol{\Sigma})$, with its covariance matrix structured using a Kac-Murdock-Szegö (KMS) matrix [5,17]. As we will see shortly, the combination of conditional independence $p(\mathbf{y}|\mathbf{y}^*, \boldsymbol{\eta}) = \prod_i p(y_i|y_i^*, \eta_i)$ and the KMS-structured covariance enables efficient optimization of the ELBO (Evidence Lower Bound) even though the distribution (2) itself cannot be directly evaluated due to the intractability of the integral. This approach ensures that even for high-dimensional problems with image-like structures of size HW, the computational complexity remains proportional to HW, making large-scale optimization feasible. We refer to the probabilistic model described in Eq.(2) as the ELBO computable discrete distribution.

By introducing a variational distribution $q(\mathbf{y}^*, \boldsymbol{\eta}|\mathbf{y}) = \{\prod_i q(y_i^*|y_i, \eta_i)\} q(\boldsymbol{\eta})$ as an approximate posterior and leveraging the ELBO computable discrete distribution, we can derive the ELBO as follows (see A.2 in Supplementary Material for details):

$$\begin{aligned}
\log p(\mathbf{y}|\mathbf{x}, \boldsymbol{\theta}) \geq{} & \mathbb{E}_{q(\mathbf{y}^*, \boldsymbol{\eta}|\mathbf{y})} \left[\log p(\mathbf{y}|\mathbf{y}^*, \boldsymbol{\eta}, \mathbf{x}, \boldsymbol{\theta}) \right] - KL\left[q(\mathbf{y}^*, \boldsymbol{\eta}|\mathbf{y}) \,\|\, p(\boldsymbol{\eta}, \mathbf{y}^*|\mathbf{x}, \boldsymbol{\theta}) \right] \\
={} & \sum_i \mathbb{E}_{q(y_i^*|y_i, \eta_i)q(\eta_i)} \left[\log p_{\boldsymbol{\theta}}(y_i^*|\mathbf{x}) \right] + \mathbb{E}_{q(\boldsymbol{\eta})} \left[\log p(\boldsymbol{\eta}) \right] \\
& - \sum_i \mathbb{E}_{q(y_i^*|y_i, \eta_i)q(\eta_i)} \left[\log q(y_i^*|y_i, \eta_i) \right] - \mathbb{E}_{q(\boldsymbol{\eta})} \left[\log q(\boldsymbol{\eta}) \right] \\
& + \sum_i \mathbb{E}_{q(y_i^*|y_i, \eta_i)q(\eta_i)} \left[\log p(y_i|y_i^*, \eta_i) \right], \tag{3}
\end{aligned}$$

where $q(\eta_i)$ is the marginal distribution of $q(\boldsymbol{\eta})$, which can be easily obtained when $q(\boldsymbol{\eta})$ follows a Gaussian distribution $q(\boldsymbol{\eta}) = \mathcal{N}(\boldsymbol{\eta}|\boldsymbol{m}, \boldsymbol{\Gamma})$. $q(y_{ik}^*|y_{ic}, \eta_i)$ and

$p(y_{ik}|y_{ic}^*, \eta_i)$ are defined as $q(y_{ik}^*|y_{ic}, \eta_i) = \delta_{kc}(1 - r(\eta_i)) + (1 - \delta_{kc})r(\eta_i)V_{kc}$, $p(y_{ik}|y_{ic}^*, \eta_i) = \delta_{kc}(1 - r(\eta_i)) + (1 - \delta_{kc})r(\eta_i)W_{kc}$, respectively. Here, δ_{kc} is the Kronecker delta, $r(\cdot)$ is the sigmoid function, and $V \in [0,1]^{|\mathcal{Y}| \times |\mathcal{Y}|}$, $\sum_{c=1}^{|\mathcal{Y}|} V_{kc} = 1$, $V_{kk} = 0$ $(k, c \in \mathcal{Y})$ represents the probability of the clean label when the given noisy label c is inconsistent with the clean label k, and $W \in [0,1]^{|\mathcal{Y}| \times |\mathcal{Y}|}$, $\sum_{c=1}^{|\mathcal{Y}|} W_{kc} = 1$, $W_{kk} = 0$ $(k, c \in \mathcal{Y})$ represents the probability of the noisy label when the given clean label c is inconsistent with the noisy label k.

Owing to the assumption of conditional independence, the expectations in the first, third, and fifth terms in the ELBO (3) are tractable, as we can sum over the possible labels for each pixel independently. The spatial correlation of label errors is incorporated through the second and fourth terms in the ELBO (3). These terms involve the trace and inverse of large matrices $\boldsymbol{\Sigma}$ and $\boldsymbol{\Gamma}$, making direct computation infeasible. However, these computational challenges are efficiently addressed by leveraging the properties of KMS-structured covariance.

3.2 KMS-structured covariance

An $n \times n$ KMS matrix R_ρ is a type of symmetric Toeplitz matrix, where each element is defined using the parameter $\rho \in (-1, 1)$. Its inverse, R_ρ^{-1}, is a tridiagonal matrix. The explicit forms of R_ρ and R_ρ^{-1} are given by:

$$R_\rho := \begin{pmatrix} 1 & \rho & \rho^2 & \cdots & \rho^{n-1} \\ \rho & 1 & \rho & \cdots & \rho^{n-2} \\ \rho^2 & \rho & 1 & \cdots & \rho^{n-3} \\ \vdots & \vdots & \vdots & \ddots & \vdots \\ \rho^{n-1} & \rho^{n-2} & \rho^{n-3} & \cdots & 1 \end{pmatrix}, \quad R_\rho^{-1} = \frac{1}{1-\rho^2}\begin{pmatrix} 1 & -\rho & 0 & \cdots & 0 \\ -\rho & 1+\rho^2 & -\rho & \cdots & 0 \\ 0 & -\rho & 1+\rho^2 & \ddots & \vdots \\ \vdots & \vdots & & \ddots & -\rho \\ 0 & 0 & \cdots & -\rho & 1 \end{pmatrix},$$

and the determinant is computed as $|R_\rho| = (1 - \rho^2)^{n-1}$. See Appendix A.1 for mathematical derivations.

This matrix is useful for representing correlations among one-dimensional variables, where the correlation decays exponentially as the index distance between two variables increases regardless of their absolute positions. Suppose a one-dimensional random variable $\mathbf{x}$ has a covariance structure given by: $\mathbb{E}[(x_i - \mu_i)(x_j - \mu_j)] = \sigma_i \sigma_j \rho^{|i-j|}$, where μ_i is the mean of x_i. By utilizing the KMS matrix R_ρ, the covariance matrix $\boldsymbol{\Sigma}$ can be expressed as $\boldsymbol{\Sigma} = V R_\rho V$ where V is a diagonal matrix whose (i, i)-th element is σ_i. Consequently, the inverse of the covariance matrix is given by $\boldsymbol{\Sigma}^{-1} = V^{-1} R_\rho^{-1} V^{-1}$.

In the case of two-dimensional spatial correlations, such as those in images, we utilize the Kronecker product. Suppose a two-dimensional random variable $\mathbf{x}$ has a covariance structure given by $\mathbb{E}[(x_{ij} - \mu_{ij})(x_{uv} - \mu_{uv})] = \sigma_{ij}\sigma_{uv}\rho^{|i-u|+|j-v|}$ where μ_{ij} is the mean of x_{ij}. Its matrix form $\boldsymbol{\Sigma}$ can be expressed as $\boldsymbol{\Sigma} = V(R_\rho \otimes R_\rho')V$. Here, we assume that the two-dimensional pixel index (i, j) can be appropriately mapped to a one-dimensional index n. V is a diagonal matrix

whose (n, n)-th element corresponds σ_{ij}, and $\otimes$ denotes the Kronecker product. Due to the properties of KMS matrices and the Kronecker product, the inverse covariance matrix is given by $\boldsymbol{\Sigma}^{-1} = V^{-1}(R_\rho^{-1} \otimes R_\rho'^{-1})V^{-1}$. Since V is a diagonal matrix and the nonzero off-diagonal elements in the inverses of the KMS matrices R_ρ and R_ρ' exist only in adjacent rows and columns, the quadratic form in the exponent of the Gaussian distribution $p(\boldsymbol{\eta}) = \mathcal{N}(\boldsymbol{\eta}|\boldsymbol{\mu}, \boldsymbol{\Sigma}) \propto \exp(-\frac{1}{2}(\boldsymbol{\eta} - \boldsymbol{\mu})^T \boldsymbol{\Sigma}^{-1}(\boldsymbol{\eta} - \boldsymbol{\mu}))$ involves only pairs of adjacent pixel variables. This structure makes the conditional distribution Markovian, meaning that, $p(\eta_i|\boldsymbol{\eta}_{\setminus i}) = p(\eta_i, \boldsymbol{\eta}_{\setminus i})/p(\boldsymbol{\eta}_{\setminus i}) \propto \exp(-\sum_{j \in \mathcal{N}_i} \Sigma_{ij}^{-1}(\eta_i - \mu_i)(\eta_j - \mu_j))$, which leads to $p(\eta_i|\boldsymbol{\eta}_{\setminus i}) = p(\eta_i|\{\eta_j|j \in \mathcal{N}_i\})$ where $\boldsymbol{\eta}_{\setminus i}$ denotes all variables in $\boldsymbol{\eta}$ except η_i, and $\mathcal{N}_i$ represents the set of adjacent pixels of i. In other words, the KMS-structured covariance matrix ensures that the Gaussian distribution retains a Markov Random Field-like property while maintaining the tractability of both the inverse and the determinant of the covariance matrix. The dependence of this conditional distribution on ρ is illustrated in Figure 1b. As shown in Figure 1b, the model can confidently infer label errors when adjacent pixels are also likely to contain label errors and the spatial correlation is strong (ρ is high), even if such errors are rare.

3.3   Optimization

For simplicity, we define N as the number of training samples, $\boldsymbol{\omega}$, as the prior distribution parameters, $\{\boldsymbol{\nu}^{(n)}\}_{n=1}^N$, as the image-specific posterior parameters, and $\mathcal{L}(\boldsymbol{\theta}, \boldsymbol{\omega}, \boldsymbol{\nu}^{(n)})$ as the negative ELBO (3) computed using these parameters. Our training algorithm is outlined in Algorithm 1, where we illustrate the case with a single sample per step, though this can be generalized to multiple samples. In each step, the model and prior parameters are updated K times, while the posterior parameters are updated M times. After training, the optimized model parameters are used to predict clean labels for new input images. Note that in Algorithm 1, the prior parameters $\boldsymbol{\omega}$ remain fixed, but with a sufficiently large training dataset, they can also be optimized.

4   Experiments

4.1   Dataset

Research on segmentation with noisy labels has been especially active in both medical imaging and satellite remote sensing. In this work, we focus on two widely used benchmark datasets that represent these domains: the JSRT dataset for medical imaging and the WHU Building dataset for satellite imagery. Detailed descriptions of each dataset are provided below.

It is common practice in noisy-label segmentation research to artificially introduce label noise for evaluation because most publicly available datasets come with clean annotations [20,31,39]. Following this convention, we also employ synthetic noise in our experiments, with details of our noise generation process described in Section 4.2.

Algorithm 1 Training loop of the model and posterior parameters optimization.

1: $\boldsymbol{\theta}, \boldsymbol{\omega}, \{\boldsymbol{\nu}_0^{(\ell)}\}_{\ell=1}^N \leftarrow$ Initialize parameters
2: **repeat**
3:     $n \leftarrow$ Randomly sample an index from $\{1, \ldots, N\}$
4:     **for** $k = 1, \ldots, K$ **do**
5:         Compute $\mathcal{L}(\boldsymbol{\theta}, \boldsymbol{\omega}, \boldsymbol{\nu}_0^{(n)})$ and its gradient with respect to $\boldsymbol{\theta}$
6:         $\boldsymbol{\theta} \leftarrow$ Update the model parameters using the gradient
7:     **end for**
8:     **for** $m = 0, 1, \ldots, M - 1$ **do**
9:         Compute $\mathcal{L}(\boldsymbol{\theta}, \boldsymbol{\omega}, \boldsymbol{\nu}_m^{(n)})$ and its gradient with respect to $\boldsymbol{\nu}_m^{(n)}$
10:        $\boldsymbol{\nu}_{m+1}^{(n)} \leftarrow$ Update the posterior parameters using the gradient
11:    **end for**
12:    $\boldsymbol{\nu}_0^{(n)} \leftarrow \boldsymbol{\nu}_M^{(n)}$
13: **until** convergence of parameters $\boldsymbol{\theta}$

JSRT Dataset [30] is a publicly available dataset provided by the Japanese Society of Radiological Technology (JSRT), which comprises chest radiographs annotated with segmentation labels for the lung fields, heart, and clavicles. All images are of size 256×256 pixels, with 199 images designated for training and 50 for testing. Following the assumption common in noisy-label segmentation research—that no clean validation data is available—we evaluated our approach using the published split of 199 training images and 50 test images. Following a previous study [20], the Clavicle region was cropped to a fixed 96×224 area for training and inference.

WHU Building Dataset [13] is a publicly available dataset for building segmentation containing satellite images of Christchurch with a resolution of $0.075\,\mathrm{m}$ covering an area of $450\,\mathrm{km}^2$. Manual annotations were provided for 22,000 buildings. The satellite images were downsampled to a resolution of $0.3\,\mathrm{m}$ and then divided into 512×512 tiles. Among the non-overlapping tiles, 4,736 were used for training, 1,036 for validation, and 2,416 for testing. Similar to JSRT, we adopted the published split for the training and testing data.

4.2 Experimental Setup

Noisy Label Settings. In the JSRT dataset, we evaluated the impact of noise caused by boundary error, which is a critical issue in the medical imaging domain [39,43]. In accordance with previous works [37,44,37,20], we employed morphological transformations as synthetic noise. As illustrated in Figure 2, the noise settings consider not only boundary ambiguities (i.e., dilation or erosion) but also affine transformations. We examined the effect of noise using α o represent the proportion of affected data and β to determine its strength, setting $\{(\alpha, \beta)\} = \{(0.3, 0.5), (0.5, 0.7), (0.7, 0.7)\}$.

In the WHU Building dataset, we modeled three types of label noise: omission noise, where labels are missing in regions that should be labeled [31,21]; commission error, where labels are present in regions that should not be due to tempo-

Fig. 2: **Examples of Noisy Labels.** In medical imaging, label noise is often simulated using morphological operations such as erosion, dilation, and affine transformations [20]. Conversely, building segmentation commonly involves omission noise, commission errors, and boundary noise [31]. The pink region indicates labels present in the noisy but absent in the clean label, while the blue region indicates the opposite.

ral changes [31]; and boundary noise, which commonly occurs in segmentation tasks [31], as illustrated in Figure 2. We define the omission ratio (ϕ), the commission ratio (ζ), and the boundary noise probability (λ) as the proportions of the total instances in the image that are perturbed by noise. Specifically, the noise parameters are set as $\{(\phi, \zeta, \lambda)\} = \{(0.1, 0.0, 0.3), (0.2, 0.05, 0.5), (0.3, 0.1, 0.7)\}$.

Baselines. We compare our method against several baselines, including cross-entropy loss (CE), noisy-label learning approaches for classification tasks (CoT [10], JoCoR [34], EM [1]), noise-robust losses for segmentation T-Loss [9], as well as techniques that account for partial spatial correlations, namely Superpixel (SP) [20] and SpatialCorrect (SC) [39]. For each method, we adopted the hyperparameters reported in the publicly available implementations or original papers, assuming them to be the best practices for their respective approaches. Although proposed method supports multi-label segmentation, many of the baseline methods are designed for binary segmentation. Therefore, in JSRT dataset, we conducted experiments by treating each class (Lung, Heart, Clavicle) as a separate binary segmentation task.

Implementation Details. We use a U-Net [28] with an EfficientNet-B0 [32] encoder, pre-trained on ImageNet [4]. The model is optimized using Adam [18] with a learning rate of 0.001 and batch sizes of 16 (JSRT) and 32 (WHU Building). The parameters in the prior $p(\boldsymbol{\eta}) = \mathcal{N}(\boldsymbol{\eta}|\boldsymbol{\mu}, \boldsymbol{\Sigma})$ and the initial values of the parameters in the variational posterior $q(\boldsymbol{\eta}) = \mathcal{N}(\boldsymbol{\eta}|\boldsymbol{m}, \boldsymbol{\Gamma})$ are set as follows. The parameters $\boldsymbol{\mu}$, the diagonal elements of $\boldsymbol{\Sigma}$, initial values of the elements of $\boldsymbol{m}$ and the diagonal elements of $\boldsymbol{\Gamma}$ are all same and denoted as μ, σ^2, m, and γ^2, respectively. These parameters were tuned using 15% of the WHU Building training set and validation sets, then fixed for all experiments, including JSRT, as follows: $\rho = 0.75$, $m = -5$, $\gamma = 1$, $\mu = -2$, and $\sigma = 1$.
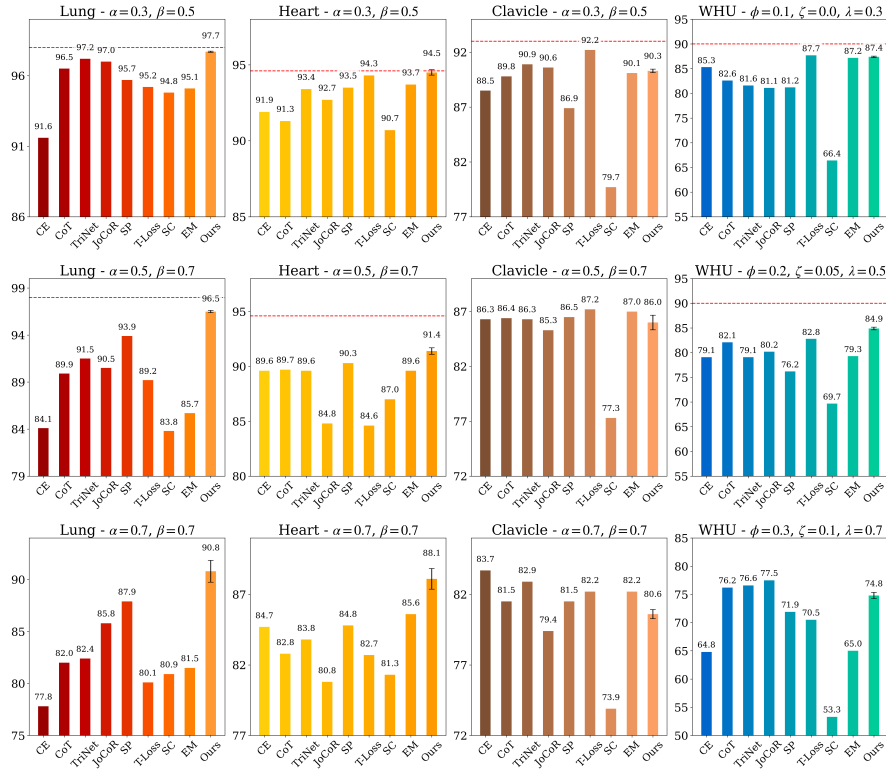
Fig. 3: **Segmentation results on JSRT and WHU Building dataset.** The first left three columns show the segmentation results for three classes—Lung, Heart, and Clavicle—in the JSRT dataset, while the right column presents the binary segmentation results for WHU Building dataset in a bar chart. The rows correspond to three different noise intensity settings tested on each dataset, with Dice scores reported for JSRT and IoU scores for WHU Building dataset.

4.3   Results for JSRT and WHU Building dataset

JSRT dataset. As shown in the first left three columns of Figure 3, we report the Dice scores for each class (Lung, Heart, Clavicle) under all three noise conditions.

Under the moderate noise condition $(\alpha, \beta) = (0.3, 0.5)$, the CE baseline, which lacks explicit noise handling, experiences a noticeable drop of 6.4%, 2.7%, and 4.5% for each organ compared to learning with clean labels. On the other hand, most noise-robust methods exhibit only minor declines. Our proposed approach, in particular, shows a very small performance degradation in Lung (only 0.3%), indicating its strong robustness to mild noise.

As the noise level increases to $(\alpha, \beta) = (0.5, 0.7)$, CE undergoes a further 13.9% performance drop, and while other baselines also suffer more substantial declines, they remain relatively more stable than CE. Notably, our method continues to perform well on the Lung and Heart classes, demonstrating a limited reduction from the noise-free scenario. For the Clavicle class—an anatomically smaller and more challenging structure—both CE and some of the noise-robust methods experience larger drops, underscoring the sensitivity of thin or complex boundaries to label perturbations.

Under the heavier noise conditions $(\alpha, \beta) = (0.7, 0.7)$, all methods face considerable accuracy degradation. Even our approach, which remains competitive or superior for the Lung and Heart, shows more pronounced drops in Clavicle segmentation. This result highlights that extremely noisy annotations—particularly for small or intricate regions—pose significant challenges. Nevertheless, compared to the other baselines, our method tends to retain higher Dice scores and lower variance in most cases.

WHU Building dataset. In the right column of Figure 3, we report IoU scores under three noise settings characterized by different omission, commission, and boundary probabilities (ϕ, ζ, λ). For moderate noise $(\phi = 0.1, \zeta = 0.0, \lambda = 0.3)$ and $(\phi = 0.2, \zeta = 0.05, \lambda = 0.5)$, CE's performance declines by 4.7% and 10.9% from the upper bound, respectively. Methods like CoT, TriNet, JoCoR, and SP generally fall into the low- to mid-80% range. T-Loss and EM display a smaller gap from the clean-label upper bound, reflecting their robust design. Notably, our method reaches 87.4% for $(\phi = 0.1, \zeta = 0.0, \lambda = 0.3)$, just 2.6% below the upper bound, and continues to outperform other baselines at the next noise level.

When the noise becomes stronger $(\phi = 0.3, \zeta = 0.1, \lambda = 0.7)$, all methods exhibit further deterioration, although CoT, TriNet, JoCoR, and SP still maintain relatively higher IoU scores. Our method remains competitive, indicating its adaptability even under substantial label corruption.

The results on the JSRT and WHU Building datasets confirm that our method effectively handles various types of label noise. In our experimental setting, this gives SC a disadvantage, as it is designed specifically for boundary-related biases.

4.4   Effect of Spatial Correlation Parameter ρ

Figure 4a shows how segmentation accuracy varies with the spatial correlation parameter ρ for JSRT Lung, JSRT Heart, JSRT Clavicle, and WHU Building datasets. In the Lung, Heart, and WHU Building datasets, performance peaks around $\rho = 0.75$, suggesting that moderate correlation effectively captures spatial structure and improves segmentation. In contrast, both ignoring spatial dependencies ($\rho = 0$) and assuming near-complete correlation ($\rho = 0.99$) result in noticeable accuracy drops. Performance on the Clavicle class differs, remaining relatively stable from $\rho = 0$ to 0.75, likely due to its smaller, elongated
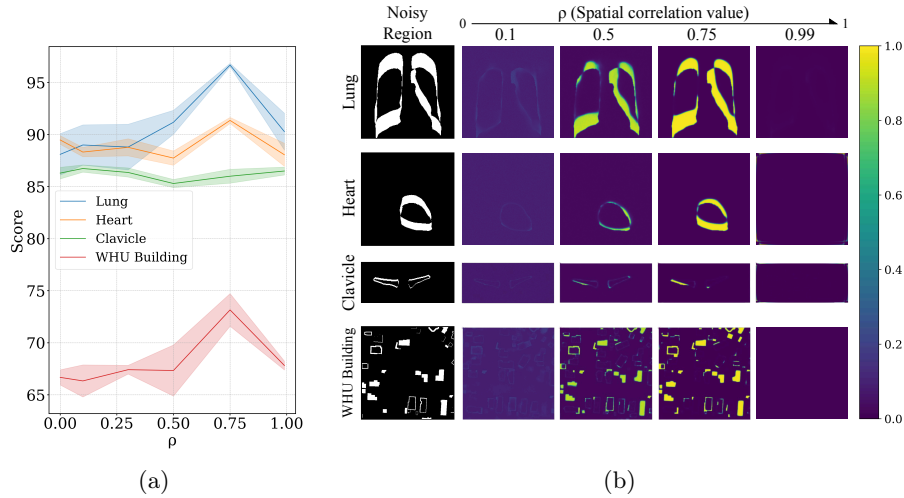
Fig. 4: **(a) Effect of ρ.** Segmentation performance was evaluated across datasets based on ρ, which represents the degree of spatial correlation, affects segmentation performance across datasets. The results show that incorporating moderate spatial correlation enhances segmentation performance. Dice scores are reported for the Lung, Heart, and Clavicle, and IoU is used for the WHU Building dataset. **(b) Estimated label error.** This figure visualizes the label error probability, computed as the sigmoid of m, the posterior mean of the logit of label error η. As shown in (a), higher accuracy in estimating η leads to better segmentation performance.

shape, which reduces the benefits of spatial correlation. Figure 4b further illustrates the estimated posterior label error probability in selected noisy regions under different ρ values. At $\rho = 0.75$, mislabeled pixels are identified more accurately, indicating that the model's label-correction mechanism is most effective under moderate correlation. In contrast, pushing ρ too high (e.g., 0.99) makes optimization unstable, leading to less reliable noise correction. Overall, these findings suggest that incorporating an appropriate level of spatial correlation significantly enhances the label correction mechanism.

5   Conclusion

We have proposed a Bayesian framework for segmentation from noisy labels, introducing the logit of the label error probability as a continuous latent variable, η. By incorporating the KMS matrix into the covariance structure of both the prior and the variational posterior distributions, our method efficiently computes the ELBO while capturing spatial correlations among adjacent pixels. This avoids the need to enumerate label combinations, improving computational efficiency. Our approach overcomes key limitations of conventional methods that

assume pixel-wise independence or only partially model spatial correlation. Experiments on medical imaging and remote sensing datasets demonstrate superior robustness to noisy annotations when the spatial correlation parameter is set to a moderate value (e.g., $\rho = 0.75$).

Our ELBO Computable Discrete Distribution extends beyond 2D segmentation to probabilistic models where priors are effectively represented by correlated discrete latent variables. Future work will explore its applications in 3D segmentation, volumetric data analysis, and other vision tasks that rely on structured priors incorporating spatial correlations.

Our method has some limitations. First, storing and optimizing posterior parameters for each training sample increases computational overhead though this cost is comparable to methods that require maintaining multiple models in memory. Second, spatial correlation may be less beneficial when the target structures are small or elongated, as the spatial dependencies may not contribute effectively.

Acknowledgments

References

1. Bekker, A.J., Goldberger, J.: Training Deep Neural-Netorks Based on Unreliable Labels. In: 2016 IEEE International Conference on Acoustics, Speech and Signal Processing (ICASSP). pp. 2682–2686 (2016)
2. Berthon, A., Han, B., Niu, G., Liu, T., Sugiyama, M.: Confidence Scores Make Instance-Dependent Label-Noise Learning Possible. In: Proceedings of the 38th International Conference on Machine Learning. Proceedings of Machine Learning Research, vol. 139, pp. 825–836 (2021)
3. Blei, D.M., Kucukelbir, A., McAuliffe, J.D.: Variational Inference: A Review for Statisticians. Journal of the American Statistical Association **112**(518), 859–877 (2017)
4. Deng, J., Dong, W., Socher, R., Li, L.J., Li, K., Fei-Fei, L.: ImageNet: A Large-Scale Hierarchical Image Database. In: 2009 IEEE Conference on Computer Vision and Pattern Recognition. pp. 248–255. IEEE (2009)
5. Fikioris, G.: Spectral Properties of Kac–Murdock–Szegö Matrices With a Complex Parameter. Linear Algebra and its Applications **553**, 182–210 (2018)
6. Foody, G.M.: Status of Land Cover Classification Accuracy Assessment. Remote Sensing of Environment **80**, 185–201 (2002)
7. Frénay, B., Verleysen, M.: Classification in the Presence of Label Noise: A Survey. IEEE Transactions on Neural Networks and Learning Systems **25**(5), 845–869 (2013)

8. Fritz, S., Mccallum, I., Schill, C., Perger, C., Grillmayer, R., Achard, F., Kraxner, F., Obersteiner, M.: Geo-Wiki.Org: The Use of Crowdsourcing to Improve Global Land Cover. Remote. Sens. **1**, 345–354 (2009)

9. Gonzalez-Jimenez, A., Lionetti, S., Gottfrois, P., Gröger, F., Pouly, M., Navarini, A.A.: Robust t-loss for Medical Image Segmentation. In: International Conference on Medical Image Computing and Computer-Assisted Intervention. pp. 714–724. Springer (2023)

10. Han, B., Yao, Q., Yu, X., Niu, G., Xu, M., Hu, W., Tsang, I., Sugiyama, M.: Co-teaching: Robust Training of Deep Neural Networks with Extremely Noisy Labels. Advances in Neural Information Processing Systems **31** (2018)

11. Henry, C., Fraundorfer, F., Vig, E.: Aerial Road Segmentation in the Presence of Topological Label Noise. In: Proceedings of the 2020 25th International Conference on Pattern Recognition (ICPR). pp. 2336–2343. IEEE (2021)

12. Huang, Z., Dumitru, C.O., Pan, Z., Lei, B., Datcu, M.: Classification of Large-Scale High-Resolution SAR Images With Deep Transfer Learning. IEEE Geoscience and Remote Sensing Letters **18**(1), 107–111 (2021)

13. Ji, S., Wei, S., Lu, M.: Fully Convolutional Networks for Multisource Building Extraction from an Open Aerial and Satellite Imagery Data Set. IEEE Transactions on Geoscience and Remote Sensing **57**(1), 574–586 (2018)

14. Jiang, Z., He, W., Kirby, M., Asiri, S., Yan, D.: Weakly Supervised Spatial Deep Learning Based on Imperfect Vector Labels With Registration Errors. In: Proceedings of the 27th ACM SIGKDD Conference on Knowledge Discovery & Data Mining. pp. 767–775 (2021)

15. Jiménez, L.G., Decaestecker, C.: Impact of Imperfect Annotations on CNN Training and Performance for Instance Segmentation and Classification in Digital Pathology. Computers in Biology and Medicine **177**, 108586 (2024)

16. Jordan, M.I., Ghahramani, Z., Jaakkola, T.S., Saul, L.K.: An introduction to variational methods for graphical models. Machine Learning **37**, 183–233 (1999)

17. Kac, M., Murdock, W.L., Szegö, G.: On the Eigen-Values of Certain Hermitian Forms. Journal of Rational Mechanics and Analysis **2**, 767–800 (1953)

18. Kingma, D.P., Ba, J.: Adam: A Method for Stochastic Optimization. arXiv preprint arXiv:1412.6980 (2014)

19. Lampert, T.A., Stumpf, A., Gâncarski, P.: An Empirical Study Into Annotator Agreement, Ground Truth Estimation, and Algorithm Evaluation. IEEE Transactions on Image Processing **25**(6), 2557–2572 (2016)

20. Li, S., Gao, Z., He, X.: Superpixel-Guided Iterative Learning from Noisy Labels for Medical Image Segmentation. In: Medical Image Computing and Computer Assisted Intervention (MICCAI 2021). pp. 525–535. Springer (2021)

21. Liu, C., Albrecht, C.M., Wang, Y., Li, Q., Zhu, X.X.: AIO2: Online correction of object labels for deep learning with incomplete annotation in remote sensing image segmentation. IEEE Transactions on Geoscience and Remote Sensing (2024)

22. Liu, S., Liu, K., Zhu, W., Shen, Y., Fernandez-Granda, C.: Adaptive Early-Learning Correction for Segmentation from Noisy Annotations. CVPR 2022 (2022)

23. Liu, Y., Zhong, Y., Ma, A., Zhao, J., Zhang, L.: Cross-resolution national-scale land-cover mapping based on noisy label learning: A case study of china. International Journal of Applied Earth Observation and Geoinformation **118**, 103265 (2023)

24. Mnih, V., Hinton, G.E.: Learning to Label Aerial Images from Noisy Data. In: Proceedings of the 29th International Conference on Machine Learning (ICML-12). pp. 567–574 (2012)

25. Patrini, G., Rozza, A., Menon, A.K., Nock, R., Qu, L.: Making Deep Neural Networks Robust to Label Noise: A Loss Correction Approach. In: 2017 IEEE Conference on Computer Vision and Pattern Recognition (CVPR). pp. 2233–2241 (2017)

26. Pelletier, C., Valero, S., Inglada, J., Champion, N., Marais-Sicre, C., Dedieu, G.: Effect of Training Class Label Noise on Classification Performances for Land Cover Mapping with Satellite Image Time Series. Remote Sensing **9**, 173 (2017)

27. Rädsch, T., Reinke, A., Weru, V., Tizabi, M.D., Schreck, N., Kavur, A.E., Pekdemir, B., Roß, T., Kopp-Schneider, A., Maier-Hein, L.: Labelling Instructions Matter in Biomedical Image Analysis. Nature Machine Intelligence **5**(3), 273–283 (2023)

28. Ronneberger, O., Fischer, P., Brox, T.: U-net: Convolutional Networks for Biomedical Image Segmentation. In: Medical Image Computing and Computer Assisted Intervention (MICCAI 2015). pp. 234–241. Springer (2015)

29. Shi, J., Wu, J.: Distilling Effective Supervision for Robust Medical Image Segmentation with Noisy Labels. In: International Conference on Medical Image Computing and Computer-Assisted Intervention. pp. 668–677. Springer (2021)

30. Shiraishi, J., Katsuragawa, S., Ikezoe, J., Matsumoto, T., Kobayashi, T., Komatsu, K.i., Matsui, M., Fujita, H., Kodera, Y., Doi, K.: Development of a Digital Image Database for Chest Radiographs With and Without a Lung Nodule: Receiver Operating Characteristic Analysis of Radiologists' Detection of Pulmonary Nodules. American Journal of Roentgenology **174**(1), 71–74 (2000)

31. Song, H., Yang, L., Jung, J.: Self-filtered Learning for Semantic Segmentation of Buildings in Remote Sensing Imagery With Noisy Labels. IEEE Journal of Selected Topics in Applied Earth Observations and Remote Sensing **16**, 1113–1129 (2022)

32. Tan, M., Le, Q.: EfficientNet: Rethinking Model Scaling for Convolutional Neural Networks. In: International Conference on Machine Learning. pp. 6105–6114. PMLR (2019)

33. Vădineanu, Ş., Pelt, D.M., Dzyubachyk, O., Batenburg, K.J.: An Analysis of the Impact of Annotation Errors on the Accuracy of Deep Learning for Cell Segmentation. In: International Conference on Medical Imaging with Deep Learning. pp. 1251–1267. PMLR (2022)

34. Wei, H., Feng, L., Chen, X., An, B.: Combating Noisy Labels by Agreement: A Joint Training Method with Co-Regularization. In: Proceedings of the IEEE/CVF Conference on Computer Vision and Pattern Recognition (CVPR) (June 2020)

35. Xia, J., Yokoya, N., Adriano, B., Broni-Bediako, C.: OpenEarthMap: A Benchmark Dataset for Global High-Resolution Land Cover Mapping. In: Proceedings of the IEEE/CVF Winter Conference on Applications of Computer Vision. pp. 6254–6264 (2023)

36. Xia, X., Liu, T., Han, B., Wang, N., Gong, M., Liu, H., Niu, G., Tao, D., Sugiyama, M.: Part-dependent Label Noise: Towards Instance-Dependent Label Noise. In: Advances in Neural Information Processing Systems. vol. 33, pp. 7597–7610 (2020)

37. Xue, C., Deng, Q., Li, X., Dou, Q., Heng, P.A.: Cascaded Robust Learning at Imperfect Labels for Chest X-ray Segmentation. In: Medical Image Computing and Computer Assisted Intervention (MICCAI 2020). pp. 579–588. Springer (2020)

38. Yang, F., Zamzmi, G., Angara, S., Rajaraman, S., Aquilina, A., Xue, Z., Jaeger, S., Papagiannakis, E., Antani, S.K.: Assessing Inter-Annotator Agreement for Medical Image Segmentation. IEEE Access **11**, 21300–21312 (2023)

39. Yao, J., Zhang, Y., Zheng, S., Goswami, M., Prasanna, P., Chen, C.: Learning to Segment from Noisy Annotations: A Spatial Correction Approach. In: International Conference on Learning Representations (2023)

40. Yao, Y., Liu, T., Han, B., Gong, M., Deng, J., Niu, G., Sugiyama, M.: Dual T: Reducing Estimation Error for Transition Matrix in Label-Noise Learning. In: Advances in Neural Information Processing Systems. vol. 33, pp. 7260–7271 (2020)
41. Zhang, L., Tanno, R., Xu, M.C., Jin, C., Jacob, J., Cicarrelli, O., Barkhof, F., Alexander, D.: Disentangling Human Error from Ground Truth in Segmentation of Medical Images. Advances in Neural Information Processing Systems **33**, 15750–15762 (2020)
42. Zhang, M., Li, W., Tao, R., Wang, S.: Transfer Learning for Optical and SAR Data Correspondence Identification With Limited Training Labels. IEEE Journal of Selected Topics in Applied Earth Observations and Remote Sensing **14**, 1545–1557 (2021)
43. Zhang, M., Gao, J., Lyu, Z., Zhao, W., Wang, Q., Ding, W., Wang, S., Li, Z., Cui, S.: Characterizing Label Errors: Confident Learning for Noisy-Labeled Image Segmentation. In: Medical Image Computing and Computer Assisted Intervention (MICCAI 2020). pp. 721–730. Springer (2020)
44. Zhang, T., Yu, L., Hu, N., Lv, S., Gu, S.: Robust Medical Image Segmentation from Non-Expert Annotations with Tri-Network. In: Medical Image Computing and Computer Assisted Intervention (MICCAI 2020). pp. 249–258. Springer (2020)

Appendix

A   Derivation details

In this section, we expand on several details that were only briefly mentioned in the main text. First, we provide a comprehensive explanation of the KMS matrix (see Section A.1). Next, we outline the intermediate steps in the derivation of the ELBO in our method and the derivation of the ELBO terms that account for spatial correlation (see Section A.2). We also derive the determinant and inverse of the covariance matrices $\boldsymbol{\Sigma}$ and $\boldsymbol{\Gamma}$, which are constructed using the KMS covariance (see Section A.3). In particular, Section A.3 details how we exploit the sparse structure of these inverses to achieve efficient computations.

A.1   KMS Matrix

The Kac–Murdock–Szegö (KMS) matrix [5,17] is defined for a positive integer $n \in \mathbb{N}$ and a parameter $\rho \in (-1, 1)$ as

$$
A_n(\rho) := \begin{bmatrix}
1 & \rho & \rho^2 & \rho^3 & \cdots & \rho^{n-1} \\
\rho & 1 & \rho & \rho^2 & \cdots & \rho^{n-2} \\
\rho^2 & \rho & 1 & \rho & \cdots & \rho^{n-3} \\
\rho^3 & \rho^2 & \rho & 1 & \ddots & \vdots \\
\vdots & \vdots & \vdots & \ddots & \ddots & \rho \\
\rho^{n-1} & \rho^{n-2} & \rho^{n-3} & \cdots & \rho & 1
\end{bmatrix} \in \mathbb{R}^{n \times n}. \tag{4}
$$

The (i, j) element of the KMS matrix is given by $\rho^{|i-j|}$, capturing the idea that the correlation between elements decays exponentially with the distance between indices.

Determinant of $A_n(\rho)$ To derive the determinant, we start with

$$
\det A_n(\rho) = \begin{vmatrix}
1 & \rho & \rho^2 & \cdots & \rho^{n-1} \\
\rho & 1 & \rho & \cdots & \rho^{n-2} \\
\rho^2 & \rho & 1 & \cdots & \rho^{n-3} \\
\vdots & \vdots & \vdots & \ddots & \vdots \\
\rho^{n-1} & \rho^{n-2} & \rho^{n-3} & \cdots & 1
\end{vmatrix}. \tag{5}
$$

For $i = 2, \ldots, n$, subtract ρ^{i-1} times the first row from the ith row. This operation zeroes out the first column (except the first row) and introduces factors of $(1 - \rho^2)$ in the diagonal of the resulting submatrix. Proceeding recursively, one obtains

$$
\det A_n(\rho) = (1 - \rho^2)^{n-1}. \tag{6}
$$

This compact expression is key for efficient computation.

Inverse of $A_n(\rho)$ The inverse is given by

$$A_n(\rho)^{-1} = \frac{1}{\det A_n(\rho)} \operatorname{adj}(A_n(\rho)), \tag{7}$$

where the adjugate $\operatorname{adj}(A_n(\rho))$ is the transpose of the cofactor matrix. Through a series of elementary row operations and by exploiting the Toeplitz structure, it can be shown that the cofactors also share a patterned structure. In particular, one finds that

$$\operatorname{adj}(A_n(\rho)) = (1 - \rho^2)^{n-2} B_n, \tag{8}$$

with

$$B_n = \begin{bmatrix} 1 & -\rho & 0 & \cdots & 0 \\ -\rho & 1+\rho^2 & -\rho & \cdots & 0 \\ 0 & -\rho & 1+\rho^2 & \ddots & \vdots \\ \vdots & \vdots & & \ddots & \ddots & -\rho \\ 0 & 0 & \cdots & -\rho & 1 \end{bmatrix}. \tag{9}$$

Thus, using $\det A_n(\rho) = (1 - \rho^2)^{n-1}$, we obtain

$$A_n(\rho)^{-1} = \frac{(1 - \rho^2)^{n-2}}{(1 - \rho^2)^{n-1}} B_n = \frac{1}{1 - \rho^2} B_n. \tag{10}$$

These derivations are essential in our framework for efficiently computing the covariance matrix inverse and determinant used in the Bayesian model.

A.2 Derivation of ELBO (Eq.(3))

We assume the following generative model for our segmentation task:

$$p_{\boldsymbol{\theta}}(\mathbf{y}^*, \mathbf{y}, \boldsymbol{\eta} | \mathbf{x}) = p_{\boldsymbol{\theta}}(\mathbf{y}^* | \mathbf{x}) \, p(\mathbf{y} | \mathbf{y}^*, \boldsymbol{\eta}) \, p(\boldsymbol{\eta}) \tag{11}$$

$$= \left\{ \prod_i p_{\boldsymbol{\theta}}(y_i^* | \mathbf{x}) \right\} \left\{ \prod_j p(y_j | y_j^*, \eta_j) \right\} p(\boldsymbol{\eta}), \tag{12}$$

where the prior $p(\boldsymbol{\eta})$ is designed to capture spatial correlation (via a KMS covariance structure).

We introduce the variational distribution $q_{\boldsymbol{\phi}}$ as

$$q_{\boldsymbol{\phi}} := q(\boldsymbol{\eta}, \mathbf{y}^* | \mathbf{y}) = q(\boldsymbol{\eta} | \mathbf{y}) \, q(\mathbf{y}^* | \boldsymbol{\eta}, \mathbf{y}) = q(\boldsymbol{\eta}) \prod_i q(y_i^* | \eta_i, y_i), \tag{13}$$

which approximates the true posterior $p_{\boldsymbol{\theta}}(\mathbf{y}^*, \boldsymbol{\eta} | \mathbf{y}, \mathbf{x})$. Then the marginal log-likelihood of the observed labels can be lower bounded as follows:

$$\log p_{\boldsymbol{\theta}}(\mathbf{y} | \mathbf{x}) = \log \int \sum_{\mathbf{y}^*} p_{\boldsymbol{\theta}}(\mathbf{y} | \boldsymbol{\eta}, \mathbf{y}^*, \mathbf{x}) \, p_{\boldsymbol{\theta}}(\boldsymbol{\eta}, \mathbf{y}^* | \mathbf{x}) \, d\boldsymbol{\eta} \tag{14}$$

$$= \log \mathbb{E}_{q_{\boldsymbol{\phi}}} \left[\frac{p_{\boldsymbol{\theta}}(\mathbf{y} | \boldsymbol{\eta}, \mathbf{y}^*, \mathbf{x}) \, p_{\boldsymbol{\theta}}(\boldsymbol{\eta}, \mathbf{y}^* | \mathbf{x})}{q_{\boldsymbol{\phi}}} \right] \tag{15}$$

$$\geq \mathbb{E}_{q_{\boldsymbol{\phi}}} [\log p_{\boldsymbol{\theta}}(\mathbf{y} | \boldsymbol{\eta}, \mathbf{y}^*, \mathbf{x})] - KL\left[q_{\boldsymbol{\phi}} \, \| \, p_{\boldsymbol{\theta}}(\boldsymbol{\eta}, \mathbf{y}^* | \mathbf{x}) \right]. \tag{16}$$

We decompose the expectation term as:

$$\mathbb{E}_{q_\phi}\left[\log p_\theta(\mathbf{y}|\boldsymbol{\eta},\mathbf{y}^*,\mathbf{x})\right] \tag{17}$$

$$= \mathbb{E}_{q_\phi}\left[\log p_\theta(\mathbf{y}|\boldsymbol{\eta},\mathbf{y}^*,\mathbf{x})\right] \tag{18}$$

$$= \mathbb{E}_{q_\phi}\left[\log p(\mathbf{y}|\boldsymbol{\eta},\mathbf{y}^*)\right] \tag{19}$$

$$= \mathbb{E}_{q_\phi}\left[\log\left(\prod_i p(y_i|\eta_i,y_i^*)\right)\right] \tag{20}$$

$$= \mathbb{E}_{q_\phi}\left[\sum_i \log p(y_i|\eta_i,y_i^*)\right] \tag{21}$$

$$= \sum_i \mathbb{E}_{q_\phi}\left[\log p(y_i|\eta_i,y_i^*)\right] \tag{22}$$

$$= \sum_i \mathbb{E}_{q(\eta_i,y_i^*|\mathbf{y})}\left[\log p(y_i|\eta_i,y_i^*)\right] \quad \text{(marginalized by } (\boldsymbol{\eta}_{\backslash i},\mathbf{y}^*_{\backslash i})) \tag{23}$$

$$= \sum_i \mathbb{E}_{q(y_i^*|\eta_i,\mathbf{y})q(\eta_i)}\left[\log p(y_i|\eta_i,y_i^*)\right] \tag{24}$$

$$= \sum_i \mathbb{E}_{q(y_i^*|\eta_i,y_i)q(\eta_i)}\left[\log p(y_i|\eta_i,y_i^*)\right], \quad (y_i^* \perp\!\!\!\perp \mathbf{y}_{\backslash i}|\eta_i,y_i) \tag{25}$$

where $\backslash i$ denotes pixel indices other than i on the image. We also decompose the negative KL divergence term as:

$$- KL\left[q_\phi\|p_\theta(\boldsymbol{\eta},\mathbf{y}^*|\mathbf{x})\right] \tag{26}$$

$$= \mathbb{E}_{q_\phi}\left[\log\frac{p_\theta(\boldsymbol{\eta},\mathbf{y}^*|\mathbf{x})}{q_\phi}\right] \tag{27}$$

$$= \mathbb{E}_{q_\phi}\left[\log p_\theta(\boldsymbol{\eta},\mathbf{y}^*|\mathbf{x}) - \log q_\phi\right] \tag{28}$$

$$= \mathbb{E}_{q_\phi}\left[\log \underbrace{p_\theta(\mathbf{y}^*|\boldsymbol{\eta},\mathbf{x})}_{= \, p_\theta(\mathbf{y}^*|\mathbf{x})}\underbrace{p_\theta(\boldsymbol{\eta}|\mathbf{x})}_{= \, p(\boldsymbol{\eta})} - \log q(\mathbf{y}^*|\mathbf{y},\boldsymbol{\eta})\underbrace{q(\boldsymbol{\eta}|\mathbf{y})}_{= \, q(\boldsymbol{\eta})}\right] \tag{29}$$

$$= \mathbb{E}_{q_\phi}\left[\log \underbrace{p_\theta(\mathbf{y}^*|\mathbf{x})}_{= \, \prod_i p_\theta(y_i^*|\mathbf{x})} + \log p(\boldsymbol{\eta}) - \log \underbrace{q(\mathbf{y}^*|\mathbf{y},\boldsymbol{\eta})}_{= \, \prod_i \{q(y_i^*|y_i,\eta_i)\}} - \log q(\boldsymbol{\eta})\right] \tag{30}$$

$$= \mathbb{E}_{q_\phi}\left[\sum_i \log p_\theta(y_i^*|\mathbf{x}) + \log p(\boldsymbol{\eta}) - \sum_i \log q(y_i^*|y_i,\eta_i) - \log q(\boldsymbol{\eta})\right] \tag{31}$$

$$= \sum_i \mathbb{E}_{q(\eta_i)q(y_i^*|\eta_i,y_i)}\left[\log p_\theta(y_i^*|\mathbf{x})\right] + \mathbb{E}_{q(\boldsymbol{\eta})}\left[\log p(\boldsymbol{\eta})\right] \tag{32}$$

$$- \sum_i \mathbb{E}_{q(\eta_i)q(y_i^*|\eta_i,y_i)}\left[\log q(y_i^*|y_i,\eta_i)\right] - \mathbb{E}_{q(\boldsymbol{\eta})}\left[\log q(\boldsymbol{\eta})\right] \tag{33}$$

Thus, the overall ELBO becomes

$$
\begin{aligned}
\log p_{\boldsymbol{\theta}}(\mathbf{y}|\mathbf{x}) \geq &\sum_i \mathbb{E}_{q(\eta_i)\,q(y_i^*|y_i,\eta_i)}\left[\log p(y_i|\eta_i,y_i^*)\right] \\
&+ \sum_i \mathbb{E}_{q(\eta_i)\,q(y_i^*|y_i,\eta_i)}\left[\log p_{\boldsymbol{\theta}}(y_i^*|\mathbf{x})\right] + \mathbb{E}_{q(\boldsymbol{\eta})}\left[\log p(\boldsymbol{\eta})\right] \\
&- \sum_i \mathbb{E}_{q(\eta_i)\,q(y_i^*|y_i,\eta_i)}\left[\log q(y_i^*|y_i,\eta_i)\right] - \mathbb{E}_{q(\boldsymbol{\eta})}\left[\log q(\boldsymbol{\eta})\right].
\end{aligned} \quad (34)
$$

A.3 Efficient ELBO Computation

In our framework, the spatially correlated prior $p(\boldsymbol{\eta})$ is modeled as a Gaussian distribution with a covariance matrix that incorporates spatial structure via a Kac–Murdock–Szegö (KMS) matrix:

$$
\boldsymbol{\Sigma} = V\left(R_\rho \otimes R'_\rho\right)V, \quad (35)
$$

where $R_\rho = A_H(\rho) \in \mathbb{R}^{H \times H}$ and $R'_\rho = A_W(\rho) \in \mathbb{R}^{W \times W}$ are the KMS matrices for the vertical and horizontal directions, respectively, and V is a diagonal matrix (e.g., $V = \sigma I$ in a simplified setting).

Because the inverse of a KMS matrix is tridiagonal, the inverse of the Kronecker product $R_\rho^{-1} \otimes R'^{-1}_\rho$ is very sparse (with at most 9 nonzero entries per row). Hence, if $V = \sigma I$, then

$$
\boldsymbol{\Sigma}^{-1} = V^{-1}\left(R_\rho^{-1} \otimes R'^{-1}_\rho\right)V^{-1} = \frac{1}{\sigma^2}(R_\rho^{-1} \otimes R'^{-1}_\rho). \quad (36)
$$

Similarly, by exploiting the determinant properties of Kronecker products,

$$
\begin{aligned}
\det \boldsymbol{\Sigma} &= (\det V)^2\,(\det R_\rho)^W (\det R'_\rho)^H \\
&= \left(\prod_{i=1}^{HW} \sigma_i\right)^2 (1-\rho^2)^{W(H-1)}(1-\rho^2)^{H(W-1)}.
\end{aligned} \quad (37)
$$

Taking the logarithm yields

$$
\log \det \boldsymbol{\Sigma} = 2\sum_{i=1}^{HW} \log \sigma_i + W(H-1)\log(1-\rho^2) + H(W-1)\log(1-\rho^2). \quad (38)
$$

The efficient computation of the trace terms in the ELBO is similarly achieved by noting that $\boldsymbol{\Sigma}^{-1}$ is sparse, which reduces the computational burden when evaluating expressions such as $\text{tr}\left(\boldsymbol{\Gamma}\boldsymbol{\Sigma}^{-1}\right)$ and $\text{tr}\left((\boldsymbol{\mu}-\boldsymbol{m})(\boldsymbol{\mu}-\boldsymbol{m})^T\boldsymbol{\Sigma}^{-1}\right)$.